Journal of Applied Physics

RESEARCH ARTICLE | FEBRUARY 23 2026

Opto-electronic and mechanical properties of $(Cd_xZn_{1-x})_2SnO_4$ in the cubic and orthorhombic phases using first-principles methods FREE

B. K C ; M. Sitaula ; V. T. Barone; S. R. Kandel ; S. V. Khare

J. Appl. Phys. 139, 085102 (2026)
https://doi.org/10.1063/5.0316837

Journal of Applied Physics ARTICLE pubs.aip.org/aip/jap

Opto-electronic and mechanical properties of $(Cd_xZn_{1-x})_2SnO_4$ in the cubic and orthorhombic phases using first-principles methods

Cite as: J. Appl. Phys. **139**, 085102 (2026); doi: 10.1063/5.0316837
Submitted: 15 December 2025 · Accepted: 3 February 2026 ·
Published Online: 23 February 2026

B. K C, M. Sitaula, V. T. Barone, S. R. Kandel, and S. V. Khare[a)]

AFFILIATIONS

Department of Physics and Astronomy, Wright Center for Photovoltaics Innovation and Commercialization (PVIC), University of Toledo, Toledo, Ohio 43606, USA

[a)]**Author to whom correspondence should be addressed:** sanjay.khare@utoledo.edu

ABSTRACT

We have computationally studied the cubic and orthorhombic $(Cd_xZn_{1-x})_2SnO_4$ alloy systems (x = 0.00, 0.25, 0.50, 0.75, and 1.00) and investigated their structural, mechanical, vibrational, and opto-electronic properties for photovoltaic applications using density functional theory and beyond methods. The calculated formation energies are below −12.41 eV for the cubic phase and −6.64 eV for the orthorhombic phase. The elastic analysis shows that the bulk moduli for both structures range from 98 to 164 GPa, shear moduli from 41 to 66 GPa, Young's moduli from 113 to 175 GPa, and the Vickers hardness from 3.18 to 8.95 GPa. All the alloy compositions are mechanically and dynamically stable. The bandgap values, calculated using the hybrid HSE06 functional, range from 1.92 to 2.85 eV and decrease with (Cd). Both structures' alloys have significantly higher hole effective mass than electron effective mass. A favorable absorption coefficient, along with reflectivity, suggests that the $(Cd_xZn_{1-x})_2SnO_4$ alloy system can be used as a transparent conducting oxide layer material for solar cell applications.

Published by AIP Publishing. https://doi.org/10.1063/5.0316837

I. INTRODUCTION

The global demand for renewable energy has increased significantly due to the depletion of non-renewable energy sources.[1] Among various renewable energy technologies, solar energy has emerged as a leading candidate. However, further improvements in photovoltaic (PV) performance, stability, and the development of new materials that can replace the toxic components and be less costly in current technologies are needed. Active research on various materials has been conducted to address these challenges. So far, CdTe-based solar cells have had an efficiency of 28%.[2,3] For better performance, a suitable material is required in transparent conducting oxide (TCO). Materials such as magnesium oxide (MgO), zinc oxide (ZnO), indium oxide (In_2O_3), and gallium oxide (Ga_2O_3) have been mostly used in this layer.[4–9] Yet, the researchers are motivated to explore alternative materials that are earth-abundant, non-toxic, low-cost, and high-performance TCO in solar cells with higher transparency and conductivity.[10] Among the promising materials are mixed metal oxides with the general formula AB_2X_4, which have potential for improving solar cell efficiency and photodetector devices.[11] Within this family, materials such as Zn_2SnO_4, Mg_2SnO_4, and Cd_2SnO_4 have attracted the attention of researchers.[10]

Numerous experimental and theoretical studies have investigated Cd_2SnO_4 and Zn_2SnO_4 because of their strong potential as TCO materials. In particular, Cd_2SnO_4 is reported to have favorable electronic properties in devices such as CdTe thin film solar cells and perovskite solar cells.[12–15] Dong *et al.* studied Cd_2SnO_4-based perovskite solar cells, achieving a power conversion efficiency of 15.58%.[13] Similarly, Matin *et al.* and Wu *et al.* reported cell efficiencies of 16.9% and 14.5%, respectively, for Cd_2SnO_4-based CdTe solar cells.[16,17] Zn_2SnO_4 is also a well-known TCO material[18] and has been an alternative material in solar cells because of its low fabrication cost and high efficiency.[19,20] Zn_2SnO_4 stands out as a widely studied material due to its wide bandgap and high electron mobility, making it suitable for applications such as gas sensors, batteries, and solar cells.[21]

Experimentally, Cd_2SnO_4 has been studied using methods such as sputtering, spray pyrolysis, solgel method, co-precipitation,

hydrothermal method, and thermal combustion.[22–27] Bhat *et al.* reported the hydrothermal synthesis of pristine Zn_2SnO_4 and copper-doped Zn_2SnO_4.[11] Gracia *et al.* reported the pressure-induced phase transformation in Zn_2SnO_4 using the CRYSTAL09 package and showed that the material is stable in a cubic inverse spinel structure.[21] Ugur *et al.* studied the structural, elastic, and electronic properties of the end members using density functional theory (DFT).[28] Allali *et al.* reported the theoretical prediction of structural, electronic, and optical properties of cubic Cd_2SnO_4 and Zn_2SnO_4 using the (FP-(L) APW + lo) approach based on DFT and implemented in the Wien2k package.[10] Despite numerous theoretical and experimental studies on these materials, a comprehensive theoretical analysis of $(Cd_xZn_{1-x})_2SnO_4$ alloys at various compositions still remains absent. At present, it is important to analyze the overall trends in the structural, mechanical, vibrational, and opto-electronic properties to evaluate the potential of the $(Cd_xZn_{1-x})_2SnO_4$ alloy system.

In this work, we performed a detailed study on $(Cd_xZn_{1-x})_2SnO_4$, such that $0 \leq x \leq 1$ in steps of $\Delta x = 0.25$ for both cubic and orthorhombic phases using DFT and beyond. As (Cd) was added, the formation energy and bandgap values decreased, consistent with previous findings. The intermediate compositions of the alloy system were investigated using the Special Quasirandom Structures (SQS) approach to see the trends in their alloy behavior. All members of the alloy, both cubic and orthorhombic, are mechanically and dynamically stable. The Crystal Orbital Hamilton Population (COHP) analysis provided bonding and antibonding interactions for the alloy system. The effective mass study shows that the hole effective mass (m_h^*) in both structures is larger than the electron effective mass (m_e^*), suggesting that electrons move as the majority charge carriers. Moreover, analysis of the absorption coefficient and reflectivity using the HSE06 functional indicates that the $(Cd_xZn_{1-x})_2SnO_4$ alloy system is a promising candidate for TCO layer applications in solar cells.

II. COMPUTATIONAL METHODS

All density functional theory (DFT) and beyond calculations were performed using the Vienna *Ab initio* Simulation Package (VASP).[29–31] The Perdew–Burke–Ernzerhof (PBE)[32] Generalized Gradient Approximation (GGA) exchange-correlation functional was implemented within the Projector-Augmented-Wave (PAW) method.[30,33,34] PAW PBE VASP pseudopotentials, i.e., "Cd," "Zn," "Sn_d," and "O," with a plane-wave energy cutoff of 450 eV and a k-point mesh of $(4 \times 4 \times 4)$ were implemented for this investigation.[35] The electronic and ionic convergence criteria were set at 10^{-6} eV and 0.01 eV/Å, respectively, with a Gaussian smearing width of 0.05 eV.[36–38] Initial crystal structures were obtained from the Materials Project.[39] To model the random occupancy of Cd and Zn in the disordered crystal, SQS[40] were generated using the mcsqs code within the Alloy Theoretical Automated Toolkit.[41] SQS models were constructed for compositions x = 0.25, 0.50, and 0.75. Multiple atomic configurations were tested for each intermediate composition to evaluate the lattice parameters and bandgaps at the GGA level, to test the reliability of the data for the SQS generated disordered structures. The observed variation in lattice constants across configurations of the same composition was minimal, with a maximum deviation of 0.04 Å, while the bandgap varied by no more than 0.04 eV. Hence, we consider these parameters to be constant and assume that other reported calculations are also constant. Therefore, a single representative structure is sufficient to accurately capture the alloy behavior. Visualization for Electronic and Structural Analysis Software (VESTA) was used to simulate powder diffraction patterns.[42]

After relaxing the positions, cell shape, and cell volume, the geometry of the crystal structures was optimized. After relaxation, the ground-state energies of the reactants and products were calculated to compute the formation energy. Formation energy per formula unit of $(Cd_xZn_{1-x})_2SnO_4$ was calculated using the following expression:[9,43,44]

$$E_{form} = E[(Cd_xZn_{1-x})_2SnO_4] - 2[xE(Cd) + (1-x)E(Zn)] - E(Sn) - 4E(O_2)/2. \quad (1)$$

E(Cd), E(Zn), E(Sn), and $E(O_2)$ are the ground-state energies of cadmium (space group: $P6_3/mmc$), zinc (space group: $P6_3/mmc$), tin (space group: $I4_1/amd$), and oxygen dimer *in vacuo*, respectively.

Elastic constants were obtained by computing the Hessian matrices of directional second derivatives of energy with respect to cell distortions using finite differences. The elastic tensor (C_{ij}) and elastic compliance tensors (S_{ij}) were further used to derive the average bulk (B) and shear (G) moduli following the Voigt–Reuss–Hill approximation equations, as described below:[45–47]

$$B_V = [C_{11} + C_{22} + C_{33} + 2(C_{12} + C_{23} + C_{31})]/9, \quad (2)$$

$$G_V = [C_{11} + C_{22} + C_{33} - C_{12} - C_{23} - C_{31}) + 3(C_{44} + C_{55} + C_{66})]/15, \quad (3)$$

$$B_R = [S_{11} + S_{22} + S_{33} + 2(S_{12} + S_{23} + S_{31})]^{-1}, \quad (4)$$

$$G_R = 15[4(S_{11} + S_{22} + S_{33} - S_{12} - S_{23} - S_{31}) + 3(S_{44} + S_{55} + S_{66})]^{-1}. \quad (5)$$

The average bulk and shear moduli are given by[48]

$$B = (B_V + B_R)/2 \text{ and } G = (G_V + G_R)/2. \quad (6)$$

Pugh's ratio (k) and Vickers hardness (H_V) were calculated using the equations recommended by Tian *et al.*[49–51] as

$$k = G/B \text{ and } H_V = 0.92k^{1.137}G^{0.708}. \quad (7)$$

Moreover, Poisson's ratio (ν) and Young's modulus (Y) were obtained using the values B and G as[52]

$$\nu = (3 - 2k)/(6 + 2k), \; Y = 9G/(3 + k). \quad (8)$$

The mechanical stability of each structure, along with its alloy system, was tested using the Born stability criteria.[53]

TABLE I. Lattice constants (a–c) in Å and formation energies per formula unit of cubic (c-) and orthorhombic (o-) $(Cd_xZn_{1-x})_2SnO_4$, computed using the GGA functional.

	c- $(Cd_xZn_{1-x})_2SnO_4$		o- $(Cd_xZn_{1-x})_2SnO_4$			
x	a (Å)	Formation energy (eV)	a (Å)	b (Å)	c (Å)	Formation energy (eV)
0.00	8.75	−14.04	6.08	6.31	8.77	−7.42
0.25	8.86	−13.53	6.17	6.38	8.94	−7.18
0.50	9.01	−13.10	6.27	6.42	9.12	−6.97
0.75	9.13	−12.75	6.36	6.49	9.26	−6.78
1.00	9.30	−12.51	6.51	6.55	9.54	−6.64

Formation energy, band structure, COHP, charge transfer, and effective mass calculations in this work were performed using the GGA functional. Both GGA and Local Density Approximation exchange-correlation functionals tend to underestimate electronic bandgaps.[54] Therefore, we applied the Heyd–Scuseria–Ernzerhof hybrid functional (HSE06), which combines 25% of the exact exchange from the Hartree–Fock theory and 75% exchange from the GGA, resulting in more accurate predictions that align with experimental results.[55,56] For better comparison, the electronic bandgaps were calculated using both GGA and HSE06 functionals. The HSE06 functional was then used to compute the electronic density of states (DOS) and dielectric response functions. Using the complex dielectric function, the absorption coefficient (α) and reflectivity (R) were calculated as $\alpha = \frac{4\pi k}{\lambda}$ and $R = \frac{(n-1)^2+k^2}{(n+1)^2+k^2}$, respectively, where the extinction coefficient (k) and refractive index (n) are given as[57–59]

$$k = \sqrt{\frac{\sqrt{\varepsilon_1^2+\varepsilon_2^2}-\varepsilon_1}{2}} \text{ and refractive index,} \tag{9}$$

$$n = \sqrt{\frac{\sqrt{\varepsilon_1^2+\varepsilon_2^2}+\varepsilon_1}{2}}. \tag{10}$$

For the analysis of chemical bonding, the Local Orbital Basis Suite Towards Electronic-Structure Reconstruction (LOBSTER) package was deployed.[60–63] Additionally, to understand charge transfer during compound formation, effective charges on each chemical species were calculated using Bader analysis.[64,65] To evaluate the phonon stability of the alloy system, the phonon DOS was computed using the Phonopy software package.[66,67]

In this work, we examine the various properties of cation-disordered $(Cd_xZn_{1-x})_2SnO_4$ as a function of concentration. Therefore, we define a bowing parameter (δ_p) that helps us understand the deviation from linearity in any physical quantity $p(x)$ such as the bandgaps, as follows:

$$p(x) = xp(1) + (1-x)p(0) - x(1-x)\delta_p, \tag{11}$$

where x is the (Cd) in the alloy system ($0 \le x \le 1$). $p(1)$ and $p(0)$ are the values of the physical quantity associated with the resultant alloys Cd_2SnO_4 and Zn_2SnO_4, respectively.

III. RESULTS

A. Structural parameters

We began our computational analysis on the $(Cd_xZn_{1-x})_2SnO_4$ alloy system in both cubic (c-) and orthorhombic (o-) phases across five different compositions (x = 0.00, 0.25, 0.50, 0.75, and 1.00). The cubic phase has a $Fd\bar{3}m$ space group with 56 atoms, whereas the orthorhombic phase has an Imma space group with 28 atoms as presented in Figs. S1–S2 in the supplementary material. Table I presents our calculated lattice parameters and formation energies for both crystal structures of the alloy system, calculated using the GGA functional. The lattice parameters of the end members are consistent with previously reported experimental results obtained through x-ray powder diffraction analysis[68] and the computational results obtained through DFT calculations.[10,21,28]

As the (Cd) is added to the alloy system, the lattice parameters of both the crystal structures increase following a nearly linear trend, consistent with Vegard's law.[69] The electronegativities of Cd and Zn are 1.46 and 1.66 e, respectively.[70] As (Cd) is added to the alloy system, the lattice parameters increase because Cd, being less electronegative than Zn, weakens bonding and leads to longer bond lengths, supported by the Bader charge analysis (Table S1 in the supplementary material) and further discussed in Sec. III C. To support this, x-ray diffraction (XRD) patterns for both the cubic and orthorhombic crystal structures across different composition ranges were simulated using VESTA, which is presented in Figs. S4(a) and S4(b) in the supplementary material. The peaks in the XRD shift to the lower angles (left) with an increase in (Cd) in

TABLE II. Elastic parameters of cubic (c-) and orthorhombic (o-) $(Cd_xZn_{1-x})_2SnO_4$. Bulk modulus (B), shear modulus (G), Young's modulus (Y), and Vickers hardness (H_V) in units of GPa, along with Pugh's ratio (k) and Poisson's ratio (ν).

	c- $(Cd_xZn_{1-x})_2SnO_4$						o- $(Cd_xZn_{1-x})_2SnO_4$					
x	B	G	Y	H_V	k	ν	B	G	Y	H_V	k	ν
0.00	164.84	56.35	151.94	4.73	0.34	0.34	157.30	66.65	175.21	6.77	0.42	0.31
0.25	157.66	50.20	136.13	4.00	0.31	0.36	149.38	59.25	157.01	5.78	0.39	0.32
0.50	152.93	46.14	125.78	3.55	0.30	0.36	98.74	58.17	145.87	8.95	0.59	0.25
0.75	151.64	43.28	118.56	3.18	0.28	0.37	143.44	48.62	131.05	4.20	0.33	0.34
1.00	138.07	41.67	113.59	3.30	0.30	0.36	131.61	46.08	123.80	4.20	0.35	0.34

the $(Cd_xZn_{1-x})_2SnO_4$ alloy system, which is consistent with the increase in lattice parameters.[9] Our simulated XRD figure is predictive. The calculated formation energies using the GGA functional are presented in Table I. Between the two crystal structures studied, the cubic phase is more stable, as indicated by its more negative formation energy (−14.04 eV for Zn_2SnO_4) compared to the orthorhombic phase (−7.42 eV). Adding the (Cd) to Zn_2SnO_4 decreases the stability within both structures. Hence, the cubic structure remains the more stable among the two, with consistently more negative formation energies across all compositions of the alloy system. Furthermore, the convex hull diagram presented in Fig. S3 in the supplementary material indicates that the alloy system

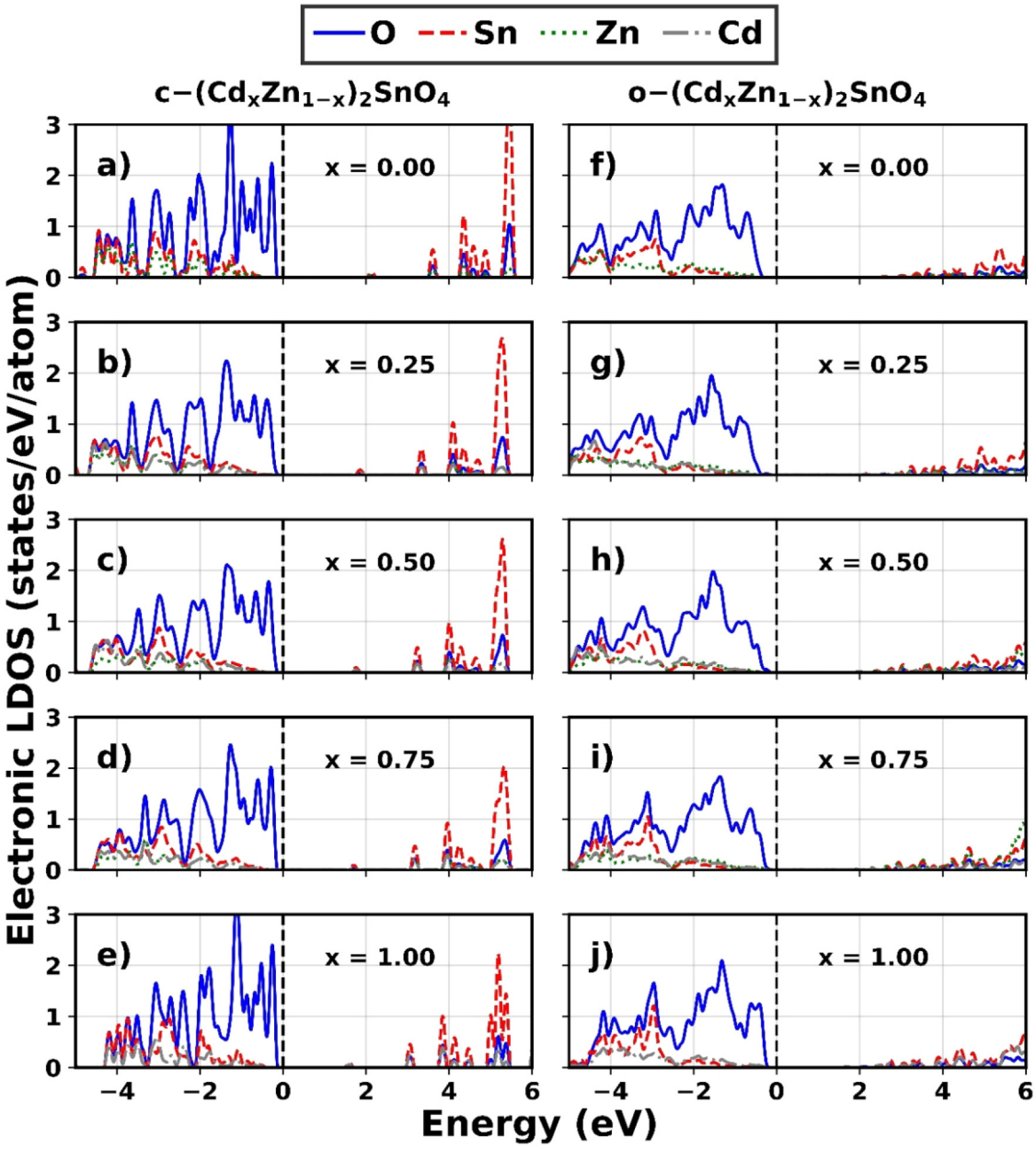

FIG. 1. Electronic local density of states (LDOS) of $(Cd_xZn_{1-x})_2SnO_4$ calculated using the HSE06 functional for the cubic phase (a)–(e) and orthorhombic phase (f)–(j) at compositions x = 0.00, 0.25, 0.50, 0.75, and 1.00. The Fermi energy is set at 0 eV.

exhibits thermodynamic stability. Hence, the $(Cd_xZn_{1-x})_2SnO_4$ alloy system is structurally and thermodynamically stable.[71,72]

B. Mechanical properties

Next, the material's strength and its stability were studied. The elastic stiffness constants (C_{ij}) were computed using the GGA functional, where the compliance tensors (S_{ij}) were obtained by taking the inverse of (C_{ij}). Equations (2–8) were employed to calculate the B, G, H_v, k, and Y as presented in Table II. The values of C_{ij} for cubic and orthorhombic structures are tabulated in Tables S4 and S5 in the supplementary material.

The bulk and shear moduli decrease with increasing (Cd) for both cubic and orthorhombic structures. However, the orthorhombic structure exhibits a non-monotonic behavior in the bulk modulus: It drops sharply to 98.74 GPa at x = 0.50, followed by a notable increase to 143.44 GPa at x = 0.75, indicating a deviation from the expected trend. This can be expected due to the bonding effects of Cd and Zn, similar to the effect that causes lattice parameters to increase with the addition of (Cd) in the alloy system. This decreasing trend in B and G can be the consequence of mechanical softening.[73]

The Pugh's criteria, $k = G/B < 0.57$, consider the material to be ductile, while those with higher k values are brittle.[74] All the alloy systems for both structures exhibit ductile characteristics, except for x = 0.50 in the orthorhombic structure, which displays a brittle nature. The Vickers hardness for both the crystal structures is relatively high, ranging from 3.18 to 8.95 GPa, which is significantly greater than that of the mostly used solar cell material, CdTe (0.49 GPa).[75] All the alloys in both the crystal structures satisfied the Born stability criteria, confirming their mechanical stability.[76] Therefore, these findings suggest that the $(Cd_xZn_{1-x})_2SnO_4$ alloy system is suitable for solar cell applications and should be studied experimentally in future studies.

C. Electronic properties

The electronic local density of states (LDOS) for both cubic (c-) and orthorhombic (o-) structures of $(Cd_xZn_{1-x})_2SnO_4$ are presented in Fig. 1 for compositions ranging from x = 0.00 to 1.00, calculated using the HSE06 functional. In both structures, the valence band maximum is dominated by oxygen (O) states attributed to 2p orbitals. The conduction band minimum is mainly governed by Sn 5s states, particularly in the 4–6 eV range. As (Cd) increases, a redistribution of Sn states within the conduction band region is observed, while Sn remains the dominant contributor to the conduction band, indicating changes in the local bonding environment due to alloying. A bowing effect is seen in the bandgap for the intermediate members of the alloy system for both structures, as presented in Fig. 2. The bowing parameter (δ_p) of the bandgap values for the cubic and orthorhombic structures are 0.42 and 0.62 eV, respectively, as obtained from Eq. (11). For the cubic structure, the bandgap decreases from 2.35 eV at x = 0.00 to 1.81 eV at x = 1.00, whereas the orthorhombic phase exhibits a similar reduction from 2.80 to 1.92 eV. This behavior is likely due to weaker Cd–O bonding and the difference in electronegativity of Cd compared to Zn. This shows how alloying affects the electronic properties, even though there is less contribution from Zn and Cd in the alloy system.

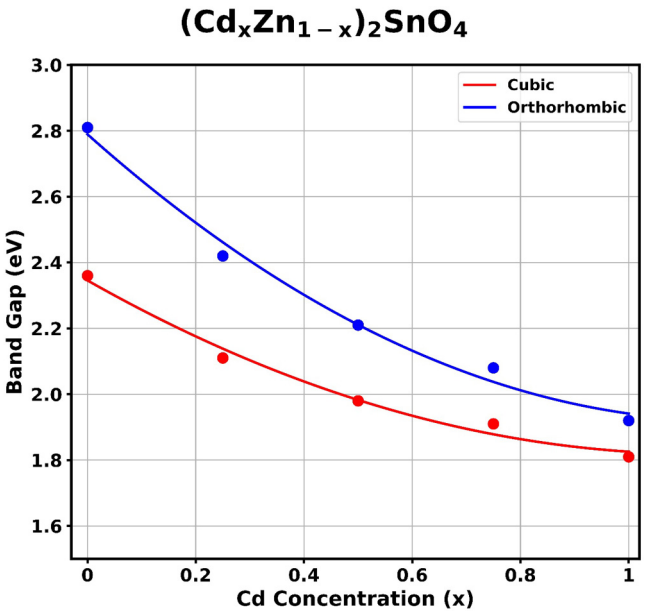

FIG. 2. Electronic bandgap values of cubic and orthorhombic $(Cd_xZn_{1-x})_2SnO_4$, calculated using the HSE06 functional. Here, the points represent computed data, and the curves are fitted based on a bowing parameter as defined in Eq. (11).

Several experimental studies have reported the bandgap values for the cubic Cd_2SnO_4, whereas an experimental bandgap for the orthorhombic is still missing. The bandgaps for cubic were reported as 2.09 and 2.59 eV using Powder x-ray diffraction (XRD) and the hydrothermal method.[77,78] Likewise, Bhat *et al.* computationally reported a 2.81 eV bandgap of cubic Zn_2SnO_4 using the Wien2k software package.[11] These results show that our computed bandgaps are consistent with the available previous results.

Bader charge analysis was used to investigate the charge transfer in the $(Cd_xZn_{1-x})_2SnO_4$ alloy system. It is the amount of negative charge in terms of elementary electronic charge (-e) transferred from Cd, Zn, and Sn to O. Table S1 in the supplementary material presents the transferred charge for all anions across the full composition range x. Within both structures, there is hardly any variation in the charges transferred in each member of the alloy system. Among the cations, Cd and Zn exhibit small charge transfer to O (~1.22–1.31 e), whereas Sn to O shows larger values (~2.12–2.30 e). All the charges transferred from each element of cations exceeds 1 e, indicating an ionic nature,[79] with the S–O bond being the most ionic. The electronegativities of Cd, Zn, Sn, and O are 1.46, 1.66, 1.72, and 3.50 e, respectively[70] with electronegativity differences of 2.04 (Cd–O), 1.85 (Zn–O), and 1.78 (Sn–O). Although the electronegativity difference in (Sn–O) is smaller compared to other bonds, the higher charge transfer in it is observed, which can be due to their bond lengths or orbital interactions, consistent with the previous observation reported by Dumre *et al.*[80]

To further elaborate on our results, we have simulated the negative projected crystal orbital Hamilton population (-pCOHP) for both structures of the $(Cd_xZn_{1-x})_2SnO_4$ alloy system using the

GGA functional to study the bonding and antibonding characteristics of the alloy system. The positive value is indicated as bonding, whereas the negative value is marked as antibonding. The study was performed to include the interactions for the first nearest neighbors of Cd–O, Zn–O, and Sn–O interactions as seen in Figs. S5(a) and S5(b) in the supplementary material. The -pCOHP analysis reveals that near the Fermi levels, no bonding is present, in contrast to the larger bonding and antibonding contributions observed at lower energies. This indicates that Cd–O, Zn–O, and Sn–O bonds are stable. Most of the COHP in the studied energy range have positive bonding with a lesser contribution to antibonding. As (Cd) is increased in the alloy system, the Cd–O population increases. To put insight into bond strength, we have further calculated the total integrated COHP values. For the cubic structure, the

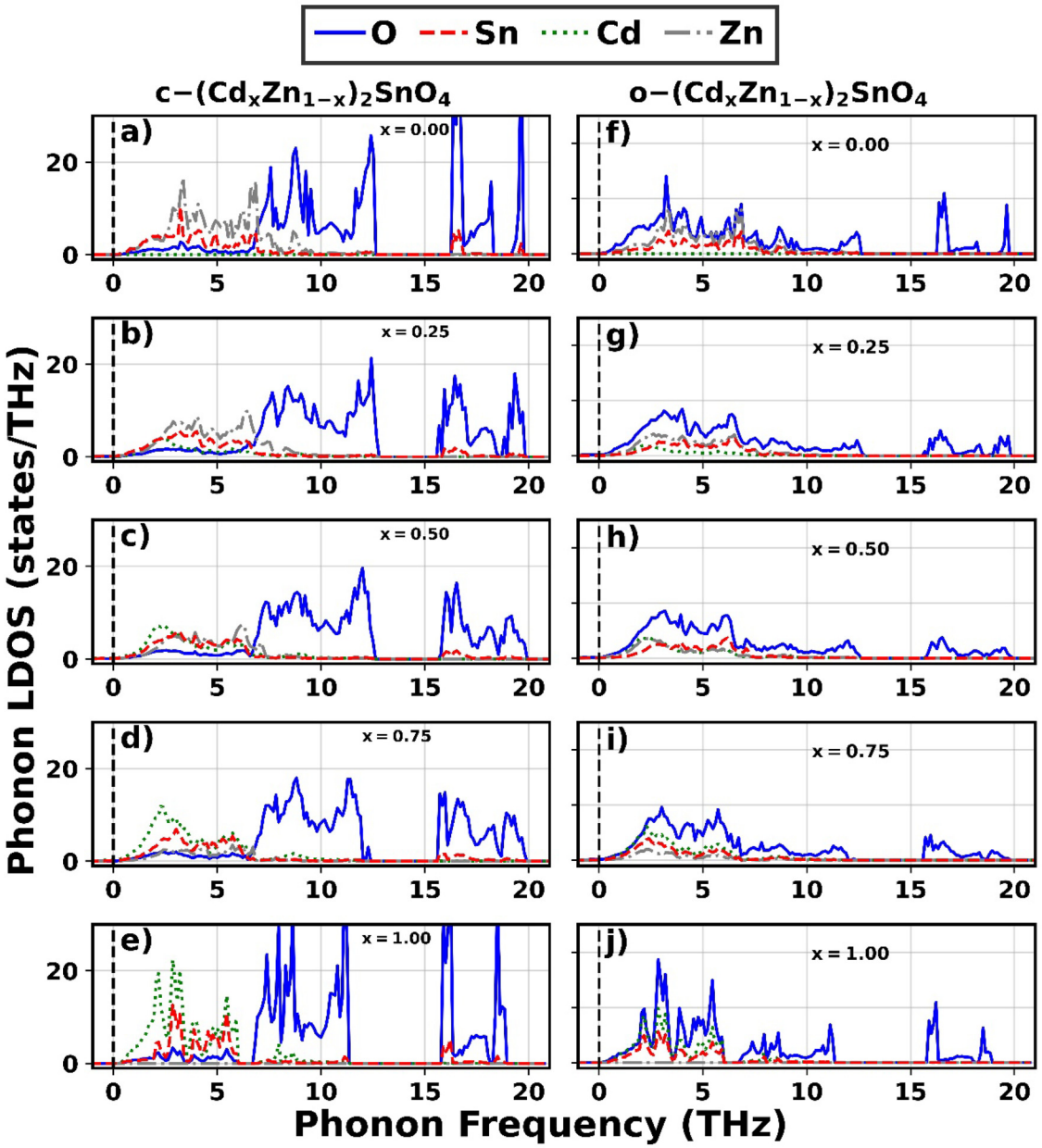

FIG. 3. Phonon local densities of states (LDOS) of $(Cd_xZn_{1-x})_2SnO_4$ calculated using the GGA functional for the cubic phase (a)–(e) and orthorhombic phase (f)–(j) at compositions x = 0.00, 0.25, 0.50, 0.75, and 1.00.

total integrated COHP for x = 0.00 has an average value of −2.12 eV, and further increasing the (Cd), its average value becomes less negative, reaching −1.97 eV at x = 1.00. Similarly, for the orthorhombic, its average value is −2.17 eV for x = 0.00 and becomes −2.00 for x = 1.00, as summarized in Table S6 in the supplementary material. These calculations show that the stability of the alloy system for both structures is reduced following a similar trend to that of the formation energy, as summarized in Table I.

To investigate the charge transport in the alloy system, we computed the effective masses using the GGA functional. For the cubic structure, a single parabolic fit at gamma gives the mass, as the curvature is isotropic. For the orthorhombic structure, m_e^* is nearly isotropic, whereas m_h^* is strongly anisotropic. Hence, m_h^* is calculated along [100], [010], and [001] directions. All the values are reported in units of the free electron rest mass (m_o). Table S2 in the supplementary material presents the average effective mass of the cubic structure. As (Cd) increases from x = 0 to 1, m_e^* decreases from 0.18 to 0.14 m_o. Segev *et al.* reported the m_e^* values of end members of the alloy system for cubic structures, i.e., Zn_2SnO_4 and Cd_2SnO_4, as 0.18 and 0.16 m_o, respectively,

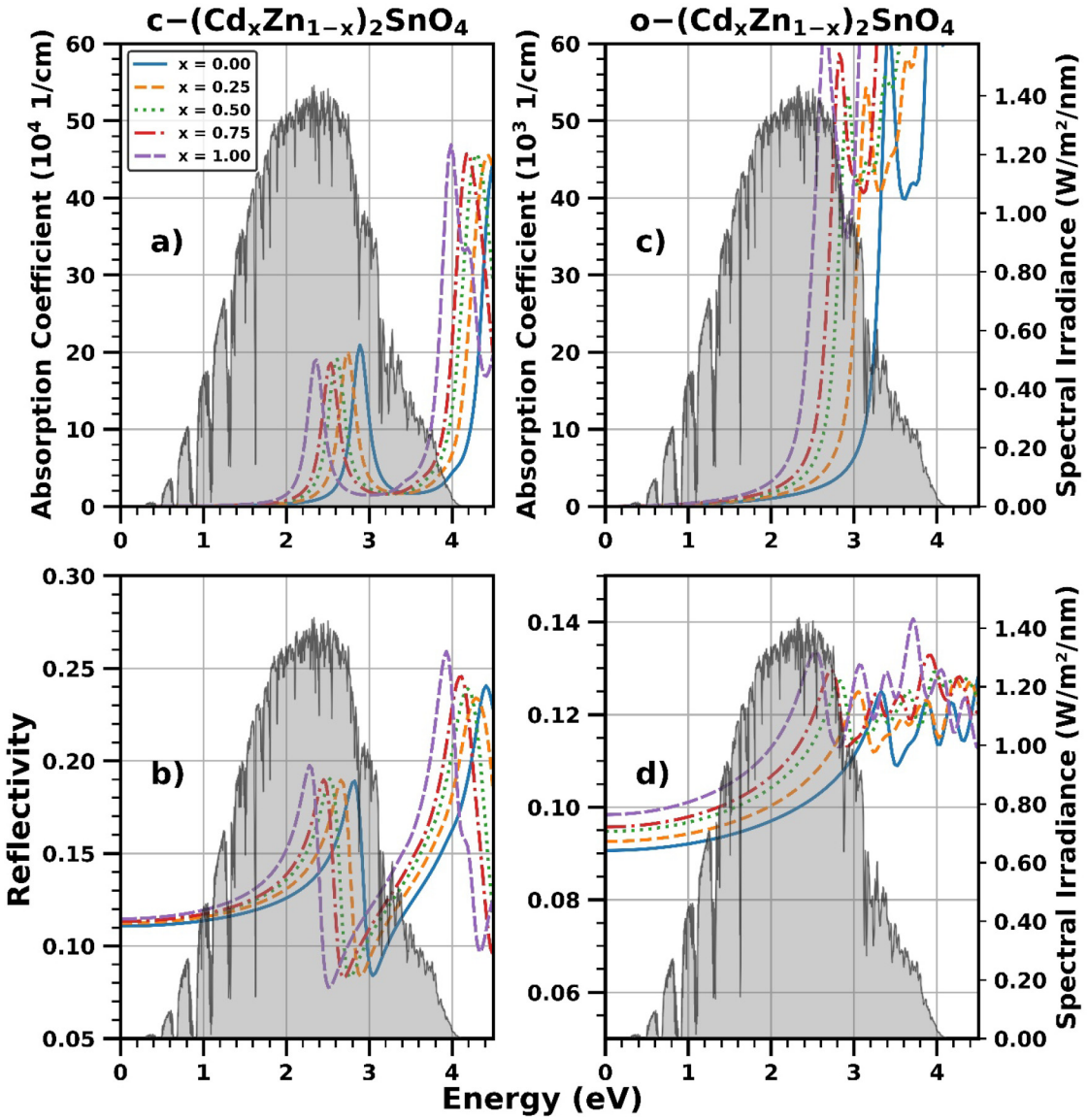

FIG. 4. Absorption coefficient and reflectivity curves of $(Cd_xZn_{1-x})_2SnO_4$ calculated using the HSE06 functional for the cubic phase (a) and (b) and orthorhombic phase (c) and (d) at compositions x = 0.00, 0.25, 0.50, 0.75, and 1.00. The shaded region represents the AM 1.5 G solar spectrum irradiance.

consistent with our findings.[81] The m_h^* values are much larger (~5–7 m_o) and vary non-monotonically across the alloy system. In the orthorhombic structure, m_e^* remains relatively light (0.33–0.28 m_o), whereas m_h^* is strongly anisotropic: m_h^* ~1.3–2.0 m_o along [100], ~7.0–16.0 m_o along [001], and ~15.0–293 m_o along [001]. These calculations were performed along a, b, and c axes following the similar approach reported by Barone *et al.* for their study on $Zn_xCd_{1-x}Te$.[82] Hence, these results indicate that in both the structures, m_h^* is significantly larger than m_e^*, suggesting that electrons are allowed to move freely as the majority charge carriers.

The charge carrier mobility calculations are done using the relation $\mu = e\tau/m^*$.[83] The cubic phase gives electron mobilities of 97.71–125.62 cm^2/V s and the hole mobilities of 2.43 –3.73 cm^2/V s. For the orthorhombic structure, the electron mobilities are 53.29–62.81 cm^2/V s; hole mobilities are directional dependent: 8.62–13.43 cm^2/V s ([100]), 1.11–2.49 cm^2/V s ([010]), and 0.06–1.11 cm^2/V s ([001]) as presented in Tables S2 and S3 in the supplementary material. Cd_2SnO_4 and Zn_2SnO_4 are well-known n-type semiconductors,[84,85] and the favorable carrier mobilities calculated in this study support their use in the TCO layer in solar cell applications.[86–88]

D. Vibrational properties

Figure 3 presents the phonon LDOS for both cubic and orthorhombic structures of $(Cd_xZn_{1-x})_2SnO_4$, computed using the GGA functional. Our calculations show that all the members of the alloy system are dynamically stable, as there is no phonon LDOS in the negative frequency region. The phonon LDOS is distributed from 0 to 20 THz. Between the two structures, the cubic structures vibrate at higher frequencies. We observe that the O phonon DOS vibrates at a higher frequency region at around 12 THz, whereas in the orthorhombic structure, it is 3 THz. The other atoms (Sn, Cd, and Zn) are found in lower frequencies compared to the O phonon DOS. It is noted that all the members of the alloy system have a wider phonon bandgap of ~4 THz in the frequency region of the stable material between 12 and 16 THz. This gap in the phonon frequency region indicates that the material can restrict sound frequencies within this region. Hence, it can be used as a candidate for applications in sound filtering and mirror applications, as it is difficult to penetrate the material from the surface.[89]

E. Optical properties

The optical properties of a material depend on the material's capacity to absorb and manage light. The absorption coefficient (α) plays a crucial role in measuring the amount of light absorbed at a certain wavelength, needed for higher solar energy conversion efficiency. This also helps to identify whether the material is clear or opaque.[90] Figure 4 presents the α and reflectivity (R) from 0 to 5 eV photon energy range of PV interest for the $(Cd_xZn_{1-x})_2SnO_4$ alloy system. The α ranges from 10^4 to 6×10^5 cm^{-1} for the cubic structure, and for the orthorhombic, it ranges from 10^3 to 6×10^4 cm^{-1}. The spectral irradiance of Air Mass 1.5 Global Spectrum is plotted in the background for better comparison.[91] The edge where α starts is its optical bandgap, corresponding to the bandgaps reported from the band structure.[92]

TABLE III. Electronic bandgaps in eV of cubic (c-) and orthorhombic (o-) $(Cd_xZn_{1-x})_2SnO_4$ computed using the GGA and HSE06 functional.

	c- $(Cd_xZn_{1-x})_2SnO_4$		o- $(Cd_xZn_{1-x})_2SnO_4$	
x	GGA (eV)	HSE06 (eV)	GGA (eV)	HSE06 (eV)
0.00	0.40	2.35	0.84	2.80
0.25	0.30	2.08	0.61	2.40
0.50	0.22	1.97	0.42	2.19
0.75	0.19	1.91	0.34	2.10
1.00	0.11	1.81	0.23	1.92

For the cubic structure, below ~1.7 eV, there is no rise in α. Beyond ~1.7 eV, α rises and reaches a maximum at around ~4 eV. For x = 0, the peak is at around ~4.4 eV. As (Cd) is added to the alloy system, the peaks shift to the left, dropping to ~4 eV for x = 1. Similarly, the orthorhombic structure has the maximum α for the alloy system between 2.8 and 3.4 eV. This trend for both structures is consistent with the bandgap reported in Table III. R measures the amount of electromagnetic radiation reflected from the material,[93] influencing its performance for solar cell applications. R at 0 eV for cubic is between 0.11 and 0.12. It shows an upward trend and reaches between 0.24 and 0.26 at ~4 eV. The orthorhombic reflectivity at 0 eV is between 0.09 and 0.10 and reaches a maximum of 0.14 at ~3.7 eV photon energy. The reflectivity within the visible region is ~18% for the cubic structures and ~13% for the orthorhombic structure. Materials with lower reflectivity are used in solar cells, which increases their efficiency.[94] The widely accepted solar cell material $CdSe_xTe_{1-x}$ has reflectivity at a range of 15%–31%, which is high compared to our material in this study.[95] Thus, the $(Cd_xZn_{1-x})_2SnO_4$ alloy system can be used as a suitable candidate for the TCO layer application in solar cells.

IV. CONCLUSION

In summary, we have computationally studied the structural, energetic, mechanical, vibrational, and opto-electronic properties of the $(Cd_xZn_{1-x})_2SnO_4$ alloy system ($0 \le x \le 1$) in both cubic ($Fd\bar{3}m$) and orthorhombic (Imma) crystal structures using DFT and beyond methods. Our results for the end members are in good agreement with the available results from experimental and theoretical studies. For the intermediate compositions, our calculations are predictive in nature due to the lack of available literature. As (Cd) increases, the bandgap values and their stability decrease. Both the structures' alloy systems have significantly higher hole effective mass than electron effective mass. According to Born stability criteria, all compositions in both cubic and orthorhombic structures are mechanically stable. Likewise, the phonon LDOS study shows no negative phonon frequencies, confirming their dynamic stability. The optical study confirmed that the material exhibits a favorable absorption coefficient and reflectivity. Hence, all the results discussed here provide valuable insights into the potential of$(Cd_xZn_{1-x})_2SnO_4$ alloy system as a TCO layer material for solar cell applications. Therefore, further research and development on this alloy system is encouraged to fully explore its potential for future applications.

SUPPLEMENTARY MATERIAL

See the supplementary material for charge transfer, effective masses, elastic constants, simulated XRD, COHP, and the band structure diagrams for the alloy system.

ACKNOWLEDGMENTS

The material is based on research sponsored by the Air Force Research Laboratory (AFRL) under Agreement No. FA9453-19-C-1002. The U.S. Government is authorized to reproduce and distribute reprints for Governmental purposes, notwithstanding any copyright notation thereon. The views and conclusions contained herein are those of the authors and should not be interpreted as necessarily representing the official policies or endorsements, either expressed or implied, of Air Force Research Laboratory or the U.S. Government. Computational work for this work was performed on the University of Toledo's computing clusters.

AUTHOR DECLARATIONS

Conflict of Interest

The authors have no conflicts to disclose.

Author Contributions

B. K C: Conceptualization (equal); Data curation (equal); Formal analysis (equal); Investigation (equal); Methodology (equal); Software (equal); Validation (equal); Visualization (equal); Writing – original draft (equal); Writing – review & editing (equal). **M. Sitaula:** Methodology (equal); Writing – review & editing (equal). **V. T. Barone:** Conceptualization (equal); Methodology (equal). **S. R. Kandel:** Methodology (equal). **S. V. Khare:** Conceptualization (equal); Funding acquisition (equal); Project administration (equal); Resources (equal); Supervision (equal); Writing – review & editing (equal).

DATA AVAILABILITY

The data that support the findings of this study are available from the corresponding author upon reasonable request.

REFERENCES

[1]N. G. F. Reaver and S. V. Khare, "Imminence of peak in US coal production and overestimation of reserves," Int. J. Coal Geol. **131**, 90 (2014).
[2]J. N. Duenow and W. K. Metzger, "Back-surface recombination, electron reflectors, and paths to 28% efficiency for thin-film photovoltaics: A CdTe case study," J. Appl. Phys. **125**, 053101 (2019).
[3]T. Ablekim, E. Colegrove, and W. K. Metzger, "Interface engineering for 25% CdTe solar cells," ACS Appl. Energy Mater. **1**, 5135 (2018).
[4]D. S. Ginley and C. Bright, "Transparent conducting oxides," MRS Bull. **25**, 15 (2000).
[5]O. Bierwagen, "Indium oxide—a transparent, wide-band gap semiconductor for (opto) electronic applications," Semicond. Sci. Technol. **30**, 024001 (2015).
[6]J. Furthmüller and F. Bechstedt, "Quasiparticle bands and spectra of Ga_2O_3 polymorphs," Phys. Rev. B **93**, 115204 (2016).
[7]K. Nomura, H. Ohta, A. Takagi, T. Kamiya, M. Hirano, and H. Hosono, "Room-temperature fabrication of transparent flexible thin-film transistors using amorphous oxide semiconductors," Nature **432**, 488 (2004).
[8]A. Dive, J. Varley, and S. Banerjee, "In_2O_3-Ga_2O_3 alloys as potential buffer layers in CdTe thin-film solar cells," Phys. Rev. Appl. **15**, 034028 (2021).
[9]B. K C, V. Barone, S. Kandel, M. Sitaula, B. Dumre, R. Ellingson, and S. Khare, "Computational investigation of structural, electronic, and optical properties of $(In_xGa_{1-x})_2O_3$ alloys as candidates for emitter layer application in solar cells," Physica B **715**, 417615 (2025).
[10]D. Allali, A. Bouhemadou, and S. Bin-Omran, "Theoretical prediction of the structural, electronic and optical properties of SnB_2O_4 (B = Mg, Zn, Cd)," Comput. Mater. Sci. **51**, 194 (2012).
[11]A. A. Bhat, I. Assadullah, A. Farooq, K. A. Malik, J. H. Malik, R. Tomar, I. Islam, A. M. Ali, and S. A. Khandy, "Band-gap alteration of Zn_2SnO_4 nanostructures for optical and photo-luminescent applications," Mater. Chem. Phys. **306**, 127993 (2023).
[12]X. Wu, "High-efficiency polycrystalline CdTe thin-film solar cells," Sol. Energy **77**, 803 (2004).
[13]D. Liu, S. Ren, X. Ma, C. Liu, L. Wu, W. Li, J. Zhang, and L. Feng, "Cd_2SnO_4 transparent conductive oxide: A promising alternative candidate for highly efficient hybrid halide perovskite solar cells," RSC Adv. **7**, 8295 (2017).
[14]D. A. Cristaldi, G. Impellizzeri, F. Priolo, T. Gupta, and A. Gulino, "Structural, electronic, and electrical properties of Y-doped Cd_2SnO_4," J. Phys. Chem. C **116**, 3363 (2012).
[15]M. M. El-Nahass, A. A. Atta, M. M. Abd El-Raheem, and A. M. Hassanien, "Structural and optical properties of DC sputtered Cd_2SnO_4 nanocrystalline films," J. Alloys Compd. **585**, 1 (2014).
[16]M. A. Matin, M. Mannir Aliyu, A. H. Quadery, and N. Amin, "Prospects of novel front and back contacts for high efficiency cadmium telluride thin film solar cells from numerical analysis," Sol. Energy Mater. Sol. Cells **94**, 1496 (2010).
[17]X. Wu, T. J. Coutts, and W. P. Mulligan, "Properties of transparent conducting oxides formed from CdO and ZnO alloyed with SnO_2 and In_2O_3," J. Vac. Sci. Technol. A **15**, 1057 (1997).
[18]F. Di Giacomo, V. Zardetto, A. D'Epifanio, S. Pescetelli, F. Matteocci, S. Razza, A. Di Carlo, S. Licoccia, W. M. M. Kessels, and T. M. Creatore, "Flexible perovskite photovoltaic modules and cells raised on atomic layer deposited compact layers and UV-irradiated TiO_2 scaffolds on plastic substrates," Adv. Energy Mater. **5**, 1 (2015).
[19]G. K. Mor, K. Shankar, M. Paulose, O. K. Varghese, and C. A. Grimes, "Use of highly-ordered TiO_2 nanotube arrays in dye-sensitized solar cells," Nano Lett. **6**, 215 (2006).
[20]M. A. Green, K. Emery, Y. Hishikawa, W. Warta, and E. D. Dunlop, "Solar cell efficiency tables (version 39)," Prog. Photovoltaics **20**, 12 (2012).
[21]L. Gracia, A. Beltrán, and J. Andrés, "A theoretical study on the pressure-induced phase transitions in the inverse spinel structure Zn_2SnO_4," J. Phys. Chem. C **115**, 7740 (2011).
[22]K. Jeyadheepan, M. Thamilselvan, K. Kim, J. Yi, and C. Sanjeeviraja, "Optoelectronic properties of RF magnetron sputtered cadmium tin oxide (Cd_2SnO_4) thin films for CdS/CdTe thin film solar cell applications," J. Alloys Compd. **620**, 185 (2015).
[23]V. Krishnakumar, K. Ramamurthi, R. Kumaravel, and K. Santhakumar, "Preparation of cadmium stannate films by spray pyrolysis technique," Curr. Appl. Phys. **9**, 467 (2009).
[24]C. J. Diliegros Godines, C. G. Torres Castanedo, R. Castanedo Pérez, G. Torres Delgado, and O. Zelaya Ángel, "Transparent conductive thin films of Cd_2SnO_4 obtained by the sol–gel technique and their use in a solar cell made with CdTe," Sol. Energy Mater. Sol. Cells **128**, 150 (2014).
[25]A. V. Sidorak, V. V. Ivanov, and A. A. Shubin, "Cadmium stannates synthesis via thermal treatment of coprecipitated salts," Mater. Sci. Appl. **2**, 1219 (2011).
[26]S. A. Kelkar, P. A. Shaikh, P. Pachfule, and S. B. Ogale, "Nanostructured Cd_2SnO_4 as an energy harvesting photoanode for solar water splitting," Energy Environ. Sci. **5**, 5681 (2012).
[27]G. Zhang, Z. Fu, Y. Wang, H. Wang, and Z. Xie, "Hierarchical microspheres: *In situ* assembly of CdS quantum dots on Cd_2 SnO_4 nanosheets with enhanced visible light photocatalytic properties," RSC Adv. **5**, 83922 (2015).

[28]G. Uğur and A. Candan, in *Structural, Elastic, Electronic and Phonon Properties of SnX_2O_4 (X = Mg, Zn, Cd) Spinel From Density Functional Theory* (American Institute of Physics, 2014), p. 190.
[29]G. Kresse and J. Furthmüller, "Efficiency of ab-initio total energy calculations for metals and semiconductors using a plane-wave basis set," Comput. Mater. Sci. **6**, 15 (1996).
[30]G. Kresse and D. Joubert, "From ultrasoft pseudopotentials to the projector augmented-wave method," Phys. Rev. B **59**, 1758 (1999).
[31]N. Jiang, J. L. Roehl, S. V. Khare, D. G. Georgiev, and A. H. Jayatissa, "An *ab initio* computational study of pure Zn_3N_2 and its native point defects and dopants Cu, Ag and Au," Thin Solid Films **564**, 331 (2014).
[32]J. P. Perdew, J. A. Chevary, S. H. Vosko, K. A. Jackson, M. R. Pederson, D. J. Singh, and C. Fiolhais, "Atoms, molecules, solids, and surfaces: Applications of the generalized gradient approximation for exchange and correlation," Phys. Rev. B **46**, 6671 (1992).
[33]P. E. Blöchl, "Projector augmented-wave method," Phys. Rev. B **50**, 17953 (1994).
[34]P. Fang, C. P. Mulligan, R. Jia, J. Shi, S. V. Khare, and D. Gall, "Epitaxial TiC_x(001) layers: Phase formation and physical properties vs C-to-Ti ratio," Acta Mater. **226**, 117643 (2022).
[35]S. R. Kandel, B. B. Dumre, D. Gall, and S. V. Khare, "Prediction of super hardness in transition metal hexa-nitrides from density functional theory computations," Materialia **25**, 101550 (2022).
[36]D. D. Le, T. S. Ngo, J.-H. Song, and S.-K. Hong, "Epitaxial growth of bandgap tunable $ZnSnN_2$ films on (0001) Al_2O_3 substrates by using a ZnO buffer," Cryst. Growth Des. **18**, 1385 (2018).
[37]D. Fang and Y. Li, "Structural, electronic, and optical properties of ZnO: $ZnSnN_2$ compounds for optoelectronics and photocatalyst applications," Phys. Lett. A **384**, 126670 (2020).
[38]I. Efthimiopoulos, Z. T. Y. Liu, M. Kucway, S. V. Khare, P. Sarin, V. Tsurkan, A. Loidl, and Y. Wang, "Pressure-induced phase transitions in the $CdCr_2$ Se_4 spinel," Phys. Rev. B **94**, 174106 (2016).
[39]A. Jain, S. P. Ong, G. Hautier, W. Chen, W. D. Richards, S. Dacek, S. Cholia, D. Gunter, D. Skinner, G. Ceder, and K. A. Persson, "Commentary: The materials project: A materials genome approach to accelerating materials innovation," APL Mater. **1**, 011002 (2013).
[40]A. Zunger, S.-H. Wei, L. G. Ferreira, and J. E. Bernard, "Special quasirandom structures," Phys. Rev. Lett. **65**, 353 (1990).
[41]A. Van De Walle, M. Asta, and G. Ceder, "The alloy theoretic automated toolkit: A user guide," Calphad **26**, 539 (2002).
[42]K. Momma and F. Izumi, "VESTA 3 for three-dimensional visualization of crystal, volumetric and morphology data," J. Appl. Crystallogr. **44**, 1272 (2011).
[43]S. R. Kandel, B. B. Dumre, D. Gall, and S. V. Khare, "Mechanical and electronic properties of transition metal hexa-nitrides in hexagonal structure from density functional theory calculations," Comput. Mater. Sci. **221**, 112084 (2023).
[44]S. V. Khare and T. L. Einstein, "Energetics of steps and kinks on Ag and Pt using equivalent crystal theory (ECT)," Surf. Sci. **314**, L857 (1994).
[45]R. Hill, "The elastic behaviour of a crystalline aggregate," Proc. Phys. Soc. Sec. A **65**, 349 (1952).
[46]A. Reuss, "Berechnung der fließgrenze von mischkristallen auf grund der plastizitätsbedingung für einkristalle," ZAMM-J. Appl. Math. Mech. **9**, 49 (1929).
[47]X. Zhou, D. Gall, and S. V. Khare, "Mechanical properties and electronic structure of anti-ReO_3 structured cubic nitrides, M_3N, of d block transition metals M: An *ab initio* study," J. Alloys Compd. **595**, 80 (2014).
[48]P. P. Gunaicha, S. Gangam, J. L. Roehl, and S. V. Khare, "Structural, energetic and elastic properties of Cu_2ZnSn $(S_xSe_{1-x})_4$ (x= 1, 0.75, 0.5, 0.25, 0) alloys from first-principles computations," Sol. Energy **102**, 276 (2014).
[49]S. R. Kandel, D. Gall, and S. V. Khare, "Density functional theory calculations of mechanical and electronic properties of $W_{1-x}Ta_xN_6$, $W_{1-x}Mo_xN_6$, and $Mo_{1-x}Ta_xN_6$ ($0 \le x \le 1$) alloys in a hexagonal structure," J. Vac. Sci. Technol. A **41**, 063112 (2023).
[50]Z. T. Y. Liu, X. Zhou, D. Gall, and S. V. Khare, "First-principles investigation of the structural, mechanical and electronic properties of the NbO-structured 3d, 4d and 5d transition metal nitrides," Comput. Mater. Sci. **84**, 365 (2014).
[51]K. Zhang, K. Balasubramanian, B. D. Ozsdolay, C. P. Mulligan, S. V. Khare, W. T. Zheng, and D. Gall, "Epitaxial NbC_xN_{1-x} (001) layers: Growth, mechanical properties, and electrical resistivity," Surf. Coat. Technol. **277**, 136 (2015).
[52]S. R. Kandel, B. B. Dumre, D. Gall, and S. V. Khare, "Investigation of hardness in transition metal hexa-nitrides in cubic structure: A first-principles study," J. Phys. Chem. Solids **171**, 111022 (2022).
[53]M. Born, "On the stability of crystal lattices. I," Math. Proc. Cambridge Philos. Soc. **36**, 160 (1940).
[54]J. Paier, M. Marsman, K. Hummer, G. Kresse, I. C. Gerber, and J. G. Ángyán, "Screened hybrid density functionals applied to solids," J. Chem. Phys. **124**, 154709 (2006).
[55]J. Heyd, G. E. Scuseria, and M. Ernzerhof, "Hybrid functionals based on a screened Coulomb potential," J. Chem. Phys. **118**, 8207 (2003).
[56]A. V. Krukau, O. A. Vydrov, A. F. Izmaylov, and G. E. Scuseria, "Influence of the exchange screening parameter on the performance of screened hybrid functionals," J. Chem. Phys. **125**, 224106 (2006).
[57]M. Sitaula, V. T. Barone, S. R. Kandel, K. C. Bhupendra, B. B. Dumre, R. J. Ellingson, and S. V. Khare, "Optoelectronic and mechanical properties of antimony sulfide selenide ternary $Sb_2(S_xSe_{1-x})_3$ alloys using first principles methods," Comput. Condens. Matter **44**, e01103 (2025).
[58]P. Dulal, M. K. Mainali, S. Chaulagain, B. Shrestha, E. Amonette, A. Shan, and N. J. Podraza, "Optical properties of fused silica glass using spectroscopic ellipsometry from 0.4 meV to 8.5 eV," Surf. Sci. Spectra **32**, 026001 (2025).
[59]D. V. Dinh, X. Lü, O. Brandt, D. Sen, O. Fairlamb, F. Peiris, F. Lima, A. Bordovalos, S. Chaulagain, and A. Shan, "Reststrahlen band and optical bandgaps in semiconducting CrN films," arXiv:2511.22484 (2025).
[60]V. L. Deringer, A. L. Tchougréeff, and R. Dronskowski, "Crystal orbital Hamilton population (COHP) analysis as projected from plane-wave basis sets," J. Phys. Chem. A **115**, 5461 (2011).
[61]S. Maintz, V. L. Deringer, A. L. Tchougréeff, and R. Dronskowski, "Analytic projection from plane-wave and PAW wavefunctions and application to chemical-bonding analysis in solids," J. Comput. Chem. **34**, 2557 (2013).
[62]R. Nelson, C. Ertural, J. George, V. L. Deringer, G. Hautier, and R. Dronskowski, "LOBSTER: Local orbital projections, atomic charges, and chemical-bonding analysis from projector-augmented-wave-based density-functional theory," J. Comput. Chem. **41**, 1931 (2020).
[63]R. Dronskowski and P. E. Bloechl, "Crystal orbital Hamilton populations (COHP): Energy-resolved visualization of chemical bonding in solids based on density-functional calculations," J. Phys. Chem. **97**, 8617 (1993).
[64]G. Henkelman, A. Arnaldsson, and H. Jónsson, "A fast and robust algorithm for Bader decomposition of charge density," Comput. Mater. Sci. **36**, 354 (2006).
[65]E. Sanville, S. D. Kenny, R. Smith, and G. Henkelman, "Improved grid-based algorithm for Bader charge allocation," J. Comput. Chem. **28**, 899 (2007).
[66]A. Togo and I. Tanaka, "First principles phonon calculations in materials science," Scr. Mater. **108**, 1 (2015).
[67]N. J. Szymanski, I. Khatri, J. G. Amar, D. Gall, and S. V. Khare, "Unconventional superconductivity in 3d rocksalt transition metal carbides," J. Mater. Chem. C **7**, 12619 (2019).
[68]M. E. Bowden and C. M. Cardile, "Structures of orthorhombic and cubic dicadmium stannate by Rietveld refinement," Powder Diffr. **5**, 36 (1990).
[69]L. Vegard, "Die konstitution der mischkristalle und die raumfüllung der atome," Z. Phys. **5**, 17 (1921).
[70]A. L. Allred and E. G. Rochow, "A scale of electronegativity based on electrostatic force," J. Inorg. Nucl. Chem. **5**, 264 (1958).
[71]A. A. Emery and C. Wolverton, "High-throughput DFT calculations of formation energy, stability and oxygen vacancy formation energy of ABO_3 perovskites," Sci. Data **4**, 170153 (2017).
[72]H. P. Beck, M. Zhou, P. Hasanovic, E. Gießelmann, and M. Springborg, "Course on the use of DFT calculations to improve understanding of phase diagrams in solid-state chemistry," J. Chem. Educ. **98**, 3207 (2021).

[73]X. Liu, Y.-Y. Chang, S. N. Tkachev, C. R. Bina, and S. D. Jacobsen, "Elastic and mechanical softening in boron-doped diamond," Sci. Rep. **7**, 42921 (2017).
[74]S. F. Pugh, "XCII. Relations between the elastic moduli and the plastic properties of polycrystalline pure metals," London, Edinburgh, Dublin Philos. Mag. J. Sci. **45**, 823 (1954).
[75]S. Cole, M. Brown, and A. F. W. Willoughby, "The microhardness of $Cd_xHg_{1-x}Te$," J. Mater. Sci. **17**, 2061 (1982).
[76]M. Born, *On the Stability of Crystal Lattices. I* (Cambridge University Press, 1940), p. 160.
[77]G. Preethi, R. Balan, S. Koppala, and H. P. Nagaswarupa, "Cubic and orthorhombic Cd_2SnO_4 microcrystals: Molten salt synthesis, phase evolution and dye degradation studies," Mater. Res. Express **6**, 105537 (2019).
[78]S. Dinesh, M. Anandan, V. K. Premkumar, S. Barathan, G. Sivakumar, and N. Anandhan, "Photocatalytic and electrochemical performance of hydrothermally synthesized cubic Cd_2SnO_4 nanoparticles," Mater. Sci. Eng. B **214**, 37 (2016).
[79]B. B. Dumre, R. J. Nelson, R. E. Irving, R. J. Ellingson, and S. V. Khare, "Trends in opto-electronic properties of $Mg_xZn_{1-x}SnN_2$ using first principles methods," Mater. Chem. Phys. **294**, 126995 (2023).
[80]B. B. Dumre, D. Gall, and S. V. Khare, "Stability, and electronic and optical properties of ternary nitride phases of $MgSnN_2$. A first-principles study," J. Phys. Chem. Solids **153**, 110011 (2021).
[81]D. Segev and S.-H. Wei, "Structure-derived electronic and optical properties of transparent conducting oxides," Phys. Rev. B **71**, 125129 (2005).
[82]V. Barone, R. J. Ellingson, and S. V. Khare, "Bandgap tuning in $Zn_xCd_{1-x}Te$ superlattices through variable atomic ordering," J. Chem. Phys. **161**, 064703 (2024).
[83]Y. Li, Y. Yi, V. Coropceanu, and J.-L. Brédas, "Optical conductivity and optical effective mass in a high-mobility organic semiconductor: Implications for the nature of charge transport," Phys. Rev. B **90**, 245112 (2014).
[84]J. H. Yu and G. M. Choi, "Current–voltage characteristics and selective CO detection of Zn_2SnO_4 and ZnO/Zn_2SnO_4, SnO_2/Zn_2SnO_4 layered-type sensors," Sens. Actuators, B **72**, 141 (2001).
[85]S. M. Al-Sofiany and H. E. Hassan, "Radiation treatment of Cd_2SnO_4 thin films prepared by RF sputtering with different preparation conditions," J. Alloys Compd. **651**, 149 (2015).
[86]H. Yanagida and M. Miyayama, *Concise Encyclopedia of Advanced Ceramic Materials* (Elsevier, 1991), p. 340.
[87]S. Calnan and A. Tiwari, "High mobility transparent conducting oxides for thin film solar cells," Thin solid films **518**, 1839 (2010).
[88]Naima, P. K. Tyagi, and V. Singh, "N-type diamane: An effective emitter layer in crystalline silicon heterojunction solar cell," Carbon Trends **9**, 100209 (2022).
[89]R. Hornreich, M. Kugler, S. Shtrikman, and C. Sommers, "Phonon band gaps," J. Phys. I **7**, 509 (1997).
[90]J. Chang, H. Chen, G. Wang, B. Wang, X. Chen, and H. Yuan, "Electronic and optical properties of perovskite compounds $MA_{1-\alpha}FA_\alpha PbI_{3-\beta}X_\beta$ (X = Cl, Br) explored for photovoltaic applications," RSC Adv. **9**, 7015 (2019).
[91]C. A. Gueymard, "The sun's total and spectral irradiance for solar energy applications and solar radiation models," Sol. Energy **76**, 423 (2004).
[92]N. V. Smith, "Photoelectron energy spectra and the band structures of the noble metals," Phys. Rev. B **3**, 1862 (1971).
[93]M. Tarekuzzaman, M. H. Ishraq, M. A. Rahman, A. Irfan, M. Z. Rahman, M. S. Akter, S. Abedin, M. A. Rayhan, M. Rasheduzzaman, M. M. Hossen, and M. Z. Hasan, "A systematic first-principles investigation of the structural, electronic, mechanical, optical, and thermodynamic properties of Half-Heusler ANiX (A = Sc, Ti, Y, Zr, Hf; X = Bi, Sn) for spintronics and optoelectronics applications," J. Comput. Chem. **45**, 2476 (2024).
[94]M. Ratul Hasan, I. A. Apon, I. Ahmed Ovi, and F.-T. Zahra, "Impact of applied pressure on tin-based cubic halide perovskite $ASnX_3$ (A = Li, Na and X = Cl, Br, and I) in reference to their optoelectronic applications," Int. J. Energy Res. **2024**, 8213804.
[95]B. B. Dumre, N. J. Szymanski, V. Adhikari, I. Khatri, D. Gall, and S. V. Khare, "Improved optoelectronic properties in $CdSe_xTe_{1-x}$ through controlled composition and short-range order," Sol. Energy **194**, 742 (2019).